Jurnal Rekayasa Mesin
p-ISSN: 1411-6863, e-ISSN: 2540-7678
Vol.20, No.3, December **2025**, hal. 498-512

Two-Degree-of-Freedom Flow-Induced Vibrations of an Elastically-Mounted Cylinder under Oscillatory Flow: A Numerical Study

Elfrida Rizky Riadini[1*], Avicenna An Nizhami[1], Padang Yanuar[1], Amran Yobioktabera[2], Muttabik Fathul Lathief[2]
[1]Mechanical Engineering Department, Politeknik Negeri Semarang,
[2]Electrical Engineering Department, Politeknik Negeri Semarang,
Jl. Prof. Soedarto, Tembalang, Kec. Tembalang, Kota Semarang, Jawa Tengah 50275
*E-mail: elfrida.rizkyriadini@polines.ac.id

Submitted: 18-11-2025; Accepted: 04-12-2025; Published: 30-12-2025

Abstract

Flow-Induced Vibration (FIV) in oscillatory flow represents a complex fluid–structure interaction that remains insufficiently explored, particularly for two-degree-of-freedom (2-DoF) systems allowing coupled inline and cross-flow motion. Previous studies have primarily focused on steady flows or limited parameter ranges, leaving a significant knowledge gap in understanding dynamic responses influenced by both reduced velocity (U_R) and Keulegan–Carpenter (KC) numbers. This study aims to numerically investigate the vibration characteristics of a 2-DoF circular cylinder subjected to oscillatory flow, emphasizing the coupling mechanism between the two motion directions under varying U_R and KC values. The research employed a numerical approach based on the Direct Forcing Immersed Boundary (DFIB) method integrated with Navier–Stokes solvers and structural motion equations. Simulations were conducted for KC values of 5–20 and U_R ranges between 5–35. The temporal integration was performed using the third-order Adams–Bashforth schemes to ensure accuracy and stability. The results reveal that lock-in phenomena occur within specific UR ranges for each KC value, with resonance peaks identified at U_R = 5 for KC = 5, U_R = 10 for KC = 10, U_R = 15 for KC = 15, and U_R = 20 for KC = 20. Increasing KC values amplify the interaction between flow and structural responses, producing multi-mode vibrations and nonlinear coupling between inline and transverse motions. Furthermore, galloping phenomena were detected at higher UR, indicating a transition from vortex-induced vibration to hydrodynamic instability. These findings contribute to a deeper understanding of FIV dynamics in oscillatory environments, offering insights for optimizing offshore structure design and wave energy harvesting devices.

Keywords: *Direct forcing immersed boundary; flow-induced vibration; Keulegan–Carpenter number; oscillatory flow; two-degree-of-freedom*

Abstrak

Getaran akibat aliran (*Flow-Induced Vibration* / FIV) pada aliran osilasi merupakan fenomena interaksi fluida-struktur yang kompleks dan masih belum banyak diteliti, terutama pada sistem dua derajat kebebasan (2-DoF) yang memungkinkan terjadinya gerak gabungan antara arah *in-line* dan *cross-flow*. Penelitian sebelumnya sebagian besar difokuskan pada kondisi aliran tunak atau parameter terbatas, sehingga masih terdapat kesenjangan pengetahuan dalam memahami respon dinamis yang dipengaruhi oleh kecepatan tereduksi (*Reduced Velocity*, U_R) dan angka Keulegan–Carpenter (KC). Penelitian ini bertujuan untuk mengkaji secara numerik karakteristik getaran silinder 2-DoF yang dikenai aliran osilasi, dengan penekanan pada mekanisme kopling antara dua arah gerak pada variasi nilai U_R dan KC. Metode penelitian dilakukan secara numerik menggunakan pendekatan *Direct Forcing Immersed Boundary* (DFIB) yang terintegrasi dengan penyelesaian persamaan Navier–Stokes dan persamaan gerak struktur. Simulasi dilakukan untuk nilai KC antara 5 hingga 20 dan U_R antara 5 hingga 35. Integrasi waktu menggunakan skema Adams–Bashforth orde tiga dan metode Dormand–Prince untuk menjaga stabilitas serta akurasi perhitungan. Hasil simulasi menunjukkan bahwa fenomena *lock-in* terjadi pada rentang U_R tertentu untuk setiap nilai KC, dengan puncak resonansi pada U_R = 5 untuk KC = 5, UR = 10 untuk KC = 10, U_R = 15 untuk KC = 15, dan U_R = 20 untuk KC = 20. Peningkatan nilai KC menghasilkan penguatan interaksi antara fluida dan struktur yang memicu getaran multi-mode dan kopling nonlinier antara gerak *in-line* dan *cross-flow*. Selain itu, fenomena *galloping* juga ditemukan pada U_R yang lebih tinggi, menunjukkan adanya transisi dari getaran akibat pusaran menuju ketidakstabilan hidrodinamik. Penelitian ini memberikan kontribusi terhadap pemahaman yang lebih mendalam mengenai dinamika FIV pada aliran osilasi, serta menawarkan wawasan untuk optimalisasi desain struktur lepas pantai dan sistem pemanen energi gelombang yang lebih efisien.

Kata kunci: Dua derajat kebebasan; getaran akibat aliran; keulegan–carpenter; metode DFIB; aliran osilasi

1. Introduction

Flow-Induced Vibration (FIV) is a fundamental and complex fluid-structure interaction phenomenon, whereby periodic vortex shedding around a rigid body triggers oscillations in the structure. Conventional FIV research has largely focused on steady flow, which has successfully mapped dynamic response characteristics, such as lock-in phenomena, mode transitions, and energy transfer mechanisms. However, in practical marine and offshore engineering applications, structures are often subjected to oscillatory flow loads, such as those induced by waves. Oscillatory flow introduces additional complexity where FIV characteristics depend not only on the reduced velocity $\boldsymbol{U_R}$, but also on the Keulegan-Carpenter (KC) number, which quantifies the ratio between the amplitude of fluid particle displacement and the diameter of the structure. The interaction between the $\boldsymbol{U_R}$ and KC parameters creates rich and nonlinear fluid-structure dynamics that have not been fully mapped, particularly for two-degree-of-freedom (2-DoF) systems that allow simultaneous transverse and inline motion.

Advances in computational methods have enabled increasingly accurate VIV simulations. Sun et al. [1] developed a mechanical model and a specialized finite element method to study rotational VIV in an eccentric cylinder at low Reynolds numbers (Re=100), revealing a significant rotational response of up to 36.7° and a "lock-in" phenomenon. For cases with wall boundaries, Wen et al. [2] advanced Smoothed Particle Hydrodynamics (SPH) modeling enhanced with particle addition and wave damping algorithms to robustly simulate VIV of cylinders near walls.

In flexible structures, Liyuan et al. [3] combined the finite element method for structures with a 2D fluid solver (Fluent) coupled via a user-defined function (UDF) program to simulate VIV in deep-sea risers, revealing nonlinear features such as multi-frequency and multi-modal vibrations. Meanwhile, Li et al. [4] investigated VIV in a rotating cylinder near a wall, concluding that the wall effect dominates the vibration response and that rotational motion amplifies this effect.

Experimental studies continue to validate VIV cases. Jang et al. [5] explored the tandem cylinder pendulum system (PSTC) and found that the dynamic response of VIV is influenced by geometric configurations, such as the shape of the upstream cylinder and the distance between cylinders. Hu et al. [6-7] conducted a comprehensive experimental study on rough risers in tandem and side-by-side configurations, revealing the coupling mechanism between interference effects and surface roughness. They found that roughness can weaken the amplitude response of the downstream riser and widen the lock-in region on the upstream riser under certain conditions.

The "VIV forever" phenomenon, where oscillation resonance occurs at all reduced velocities even with high structural damping, was confirmed through water channel experiments and reduced-order models (ROM) [8]. Another study by Qin et al. [9] focused on frequency lock-in in hydrofoils, showing that the lock-in frequency range narrows with increasing mass ratio and initial angle of attack.

The use of VIV for energy harvesting is a rapidly developing field. Several studies have proposed innovative concepts to improve efficiency. One of these is the use of a non-linear pendulum to excite the cylinder auto parametrically, achieving higher oscillation amplitudes in the lock-in region for energy harvesting [10]. Hybrid approaches have also been introduced, such as that proposed by Huang et al. [11], which combines VIV and galloping on a bluff body with a specific angle of attack, resulting in an increase in output voltage of up to 153.5% compared to conventional galloping harvesters.

On the other hand, devices that combine vibration suppression and energy harvesting have also been developed. Li et al. [12] proposed an electromagnetic Nonlinear Energy Sink (NES) that can simultaneously dampen vibrations and

harvest energy from VIV. Fan et al. [13] investigated D-shaped prisms for VIVACE devices, finding that the angle of attack affects the vibration response and that energy conversion efficiency can reach a maximum of 11.75%.

In addition to harvesting energy, controlling and damping destructive VIV is also very important. Liu et al. [14] investigated the effectiveness of NES optimized with Particle Swarm Optimization (PSO) to suppress wind-vortex vibrations in deep-sea jacket pipes, analyzing the influence of parameters and installation positions. Basta et al. [15] evaluated linear vibration absorbers to control nonlinear VIV in airfoil structures during the lock-in phase, demonstrating high sensitivity of the frequency response to absorber parameters. Other aerodynamic strategies, such as the use of vortex isolation plates with varying opening ratios on bridges, have also been shown to be effective in suppressing torsional and heaving VIV [16].

Several studies have examined VIV under complex flow conditions. Islam et al. [17] explored energy harvesting from simple cylindrical VIV using a piezoelectric translator, analyzing power output against variations in reduced velocity and resistance. Li et al. [18] investigated VIV in a flexible riser carrying severe slug flow, finding that its VIV characteristics were significantly different from those of a riser with straight flow, including multi-mode responses triggered by slug flow. Research by Huang et al. [19] focused on modeling fluid forces and VIV characteristics in cylinders in oscillatory flow with non-zero average velocity, testing the applicability of the Morison equation model, and revealing various response regimes based on the KC number.

Based on previous research, it has been identified that most numerical studies of oscillatory flow are often limited to specific Reynolds numbers or focus on 1-DoF systems. Meanwhile, experimental research on 2-DoF systems under these conditions faces significant technical and cost constraints. Therefore, comprehensive VIV behavior of 2-DoF systems under simultaneous variations of reduced velocity ($\boldsymbol{U_R}$) and KC number parameters over a wide range remains largely unexplored. Therefore, this study conducts a systematic numerical investigation of the 2-DoF vibration response (inline and cross-flow) of a cylinder traversed by an oscillatory flow with variations in $\boldsymbol{U_R}$ and KC. This study aims to analyze the fluid-structure interaction mechanism underlying lock-in at various combinations of $\boldsymbol{U_R}$ and KC at Re=100, as well as to identify and explain the unique characteristics that arise from the coupling between inline and cross-flow motion in an oscillatory flow environment. The findings from this research are expected to provide a more in-depth and predictive understanding for the design of more reliable offshore structures and wave energy harvesting systems.

2. Material and Method

2.1. Numerical Method

The method described in this section was implemented using a numerical code written in Fortran. This code was designed to address both fluid flow and structural dynamic motion. It consists of three primary modules: pre-processing, solver, and post-processing. These modules were integrated into a single program, enabling mesh generation during the pre-processing stage, the solution of fluid and structural dynamics in the solver stage, and the storage of computed results into files during the post-processing stage. A previous study validated both the numerical method and the Fortran code adopted here, and included a comprehensive mesh-independence study to ensure solution accuracy [20-21].

A key relation employed to ensure mass conservation is the continuity equation. For incompressible fluids in a two-dimensional domain, this equation is expressed mathematically as Equation (1).

$$\nabla \cdot u = 0 \tag{1}$$

The momentum equation serves as a fundamental relation to enforce the conservation of fluid momentum. Within Eulerian grid-based formulations, under the assumption of incompressibility, this equation is expressed as Equation (2).

$$\frac{\partial \mathrm{u}}{\partial t} + (\mathrm{u} \cdot \nabla)\mathrm{u} = -\frac{\nabla p}{\rho} + \frac{1}{Re}\nabla^2 \mathrm{u} + \mathrm{f} \tag{2}$$

To determine the initial acceleration corresponding to the first intermediate velocity, the convective and diffusive terms in the momentum equation must be combined. This is achieved by summing these terms as expressed in Equation (3).

$$\frac{\partial \mathrm{u}^*}{\partial t} = -(\mathrm{u} \cdot \nabla)\mathrm{u} + \frac{1}{Re}\nabla^2 \mathrm{u} \tag{3}$$

The first intermediate velocity is obtained by applying temporal integration to Eq. (3), using the third-order Adams–Bashforth scheme explicitly, as defined in Equation (4).

$$\mathrm{u}^* = \mathrm{u}^n + \Delta t \left[\frac{23}{12}\, a^n - \frac{16}{12} a^{n-1} + \frac{5}{12} a^{n-2}\right] \tag{4}$$

In this formulation, the temporal increment Δt is applied in computing the first intermediate velocity (u^*). The computation accounts for the rate of change of u^* at the current time step (a^n), the preceding step (a^{n-1}), and the step prior to that (a^{n-2}). Since this first intermediate velocity does not yet satisfy the divergence-free condition, the Poisson equation, given in Equation (5), is subsequently solved to obtain the pressure and thus determine the second intermediate velocity.

$$\frac{\nabla \cdot \mathrm{u}^*}{\Delta t} = \frac{\nabla^2 p^{n+1}}{\rho} \tag{5}$$

The second intermediate velocity, u^{**}, is obtained through the application of Equation (6).

$$\mathrm{u}^{**} = \mathrm{u}^* - \frac{\Delta t}{\rho}\nabla p \tag{6}$$

Following the solution of Equation (6), the Direct Forcing Immersed Boundary (DFIB) method is applied to determine the velocity at the next time step, $u^{(n+1)}$, by introducing a virtual force term, as illustrated in Figure 1. This is carried out through the incorporation of Equation (7) into the momentum equation.

$$\mathrm{f}^{t+1} = \eta \, \frac{\mathrm{u_s} - \mathrm{u}^{**}}{\Delta t} \tag{7}$$

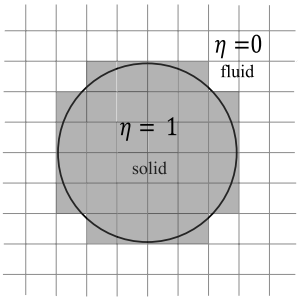

Figure 1. Discrete cell of the DFIB method on a cartesian mesh

Within the DFIB framework, the term $f^{(n+1)}$ denotes the virtual force incorporated into the momentum equation to represent the influence of the numerical forcing term. The solid-body velocity vector, u_s, specifies the velocity of the solid boundary inside the fluid domain, while the solid-body function, η, identifies whether a given point lies within a solid or fluid region. The velocity u^{**} is then advanced to $u^{(n+1)}$ through Equation (8), which defines the integration of the virtual force into the momentum equation.

$$\mathrm{u}^{n+1} = \mathrm{u}^{**} + \Delta t \mathrm{f}^{n+1} \tag{8}$$

The transverse motion of the cylinders is described by a separate differential equation, presented in Equation (9) , which characterizes their dynamic response. This equation is applied following the completion of the fluid simulation.

$$\begin{aligned} \frac{d^2x}{dt^2} + \frac{4\pi\zeta}{U_R}\frac{dx}{dt} + \frac{4\pi^2}{(U_R)^2}x &= \frac{2C_D}{\pi\, m^*} \\ \frac{d^2y}{dt^2} + \frac{4\pi\zeta}{U_R}\frac{dy}{dt} + \frac{4\pi^2}{(U_R)^2}y &= \frac{2C_L}{\pi\, m^*} \end{aligned} \tag{9}$$

The drag and lift force coefficients, C_D and C_L, are the dimensionless representations of the drag and lift forces, respectively, as defined in Equations (10) and (11).

$$\begin{aligned} F_x &= \iiint f_x \, dV \\ F_y &= \iiint f_y \, dV \end{aligned} \tag{10}$$

$$C_D = \frac{2F_x}{\rho U_\infty^2 D^2}$$
$$C_L = \frac{2F_y}{\rho U_\infty^2 D^2} \quad (11)$$

To perform the temporal integration for determining the velocity and displacement of the cylinder, the Adam-Bashforth-Moulton is employed. In this approach, the function evaluations at each stage are computed using the set of equations provided in Equations (12) and (13).

$$\frac{dx^{n+1}}{dt} = \frac{dx^n}{dt} + \frac{1}{12}\Delta t\left(23\frac{d^2x^n}{dt^2} - 16\frac{d^2x^{n-1}}{dt^2} + 5\frac{d^2x^{n-2}}{dt^2}\right)$$
$$x^{n+1} = x^n + \frac{1}{12}\Delta t\left(5\frac{dx^{n+1}}{dt} + 8\frac{dx^n}{dt} - \frac{dx^{n-1}}{dt}\right) \quad (12)$$

$$\frac{dy^{n+1}}{dt} = \frac{dy^t}{dt} + \frac{1}{12}\Delta t\left(23\frac{d^2y^n}{dt^2} - 16\frac{d^2y^{n-1}}{dt^2} + 5\frac{d^2y^{n-2}}{dt^2}\right)$$
$$y^{n+1} = y^t + \frac{1}{12}\Delta t\left(5\frac{dy^{n+1}}{dt} + 8\frac{dy^n}{dt} - \frac{dy^{n-1}}{dt}\right) \quad (13)$$

2.2. Computational Domain

Figure 2 illustrates the computational domain employed for simulating flow past a circular cylinder. The domain has a rectangular configuration with dimensions of $\mathbf{50}\boldsymbol{D} \times \mathbf{50}\boldsymbol{D}$, where $\boldsymbol{D}$ denotes the cylinder diameter. The cylinder is positioned $\mathbf{25}\boldsymbol{D}$ from the left boundary, and the flow is modeled in two dimensions. The figure highlights the placement of the computational domain within a region characterized by relatively uniform oscillatory flow.

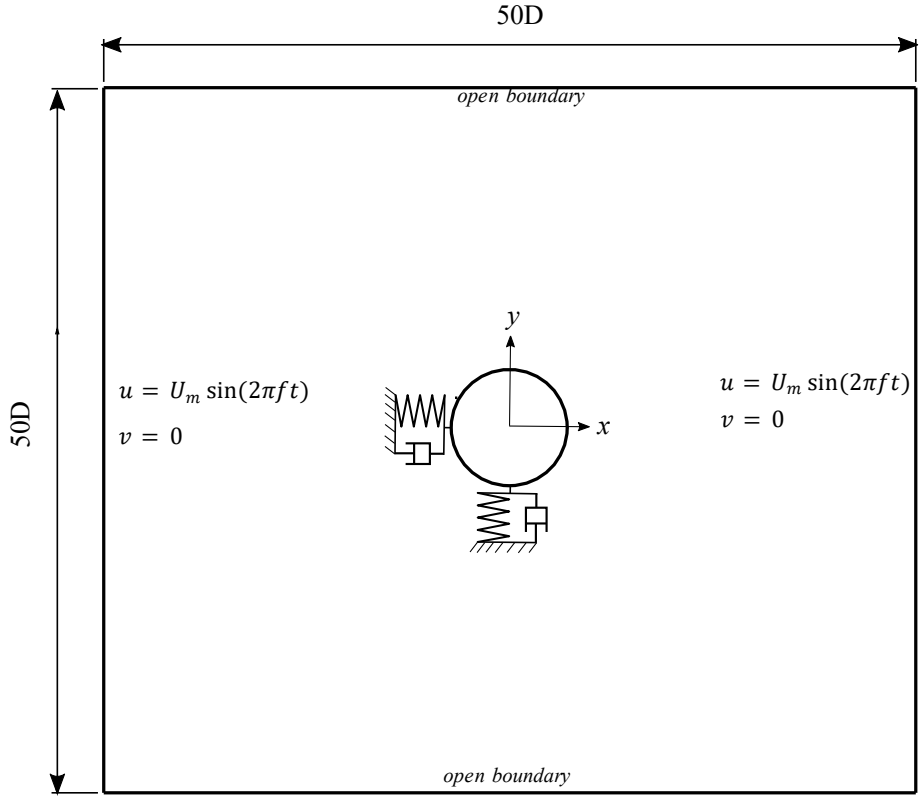

Figure 2. Computational domain of the numerical study

An axisymmetric boundary condition was imposed on both the upper and lower boundaries of the computational domain. To accurately capture the flow dynamics, a Dirichlet velocity boundary condition was prescribed at the left boundary, defined as the inlet, with specified values appropriate to the simulation setup. At the right boundary, an open boundary condition was applied, designating it as the outlet.

3. Results and Discussion

This section presents and analyzes the numerical results obtained from simulations of the two-degree-of-freedom (2-DoF) flow-induced vibration (FIV) of a circular cylinder subjected to oscillatory flow. The discussion is organized to illustrate the dynamic behavior of the cylinder under varying Keulegan–Carpenter (KC) numbers and reduced velocity (UR) values. The first part discusses the time history of drag and lift force coefficient namely, $\boldsymbol{C_D}$ and $\boldsymbol{C_L}$ for various KC values. The second part examines the time-history responses of in-line and transverse displacements for several KC values to identify the occurrence of lock-in phenomena and vibration characteristics. The third part focuses on the variation of maximum vibration amplitude with respect to UR for different KC numbers, highlighting the transition from Vortex-Induced Vibration (VIV) to galloping behavior. Galloping is characterized by a progressive increase in vibration amplitude accompanied by a decrease in vibration frequency as the reduced velocity ($\boldsymbol{U_R}$) increases. Through this organization, both temporal and parametric effects on the structural response are comprehensively discussed to elucidate the coupling mechanisms between the flow and the structure.

3.1. Time History of Force Coefficient for Various KC Number

Figure 3 shows the time history of drag force ($\boldsymbol{C_D}$) and lift force ($\boldsymbol{C_L}$) at four KC values. Based on Figure 3, it can be analyzed that variations in the KC number significantly affect the characteristics of the drag coefficient ($\boldsymbol{C_D}$) and lift coefficient ($\boldsymbol{C_L}$) in oscillatory flow around a circular cylinder. At KC=5, the drag coefficient reaches its highest value with a relatively sinusoidal signal shape, indicating the dominance of inertial forces where vortices have not yet fully formed and interact directly with the cylinder during the return flow cycle. Meanwhile, the lift coefficient in this condition shows a very low amplitude with random fluctuations, indicating the absence of regular vortex shedding as shown in Figure 4(a). As KC increases to 10, the amplitude of $\boldsymbol{C_D}$ decreases significantly accompanied by waveform distortion, while $\boldsymbol{C_L}$ shows a dramatic increase with the emergence of clear periodic components, reflecting a critical transition to the regime of asymmetric vortex formation as depicted in Figure 4(b).

At higher KC values (15 and 20), the downward trend in $\boldsymbol{C_D}$ due to the decrease in value of the oscillatory flow acceleration, marked by increasingly distorted and non-sinusoidal waveforms. On the other hand, the lift coefficient reaches its maximum value in this KC range with large-amplitude periodic signals, Fig. (4c) and (4d) confirming the full development of stable vortex shedding phenomena. Overall, the data show a transition of the flow regime from vortex shedding (KC=5) to full vortex shedding (KC=15-20). The main technical implication lies in the need for special consideration of medium-high KC conditions (10-20) in offshore structure design, where large periodic lift forces have the potential to trigger critical VIV for fatigue analysis. These findings emphasize the importance of using specific oscillatory flow hydrodynamic coefficients in the Morison Equation, given the inaccuracies that may arise when using steady flow coefficients.

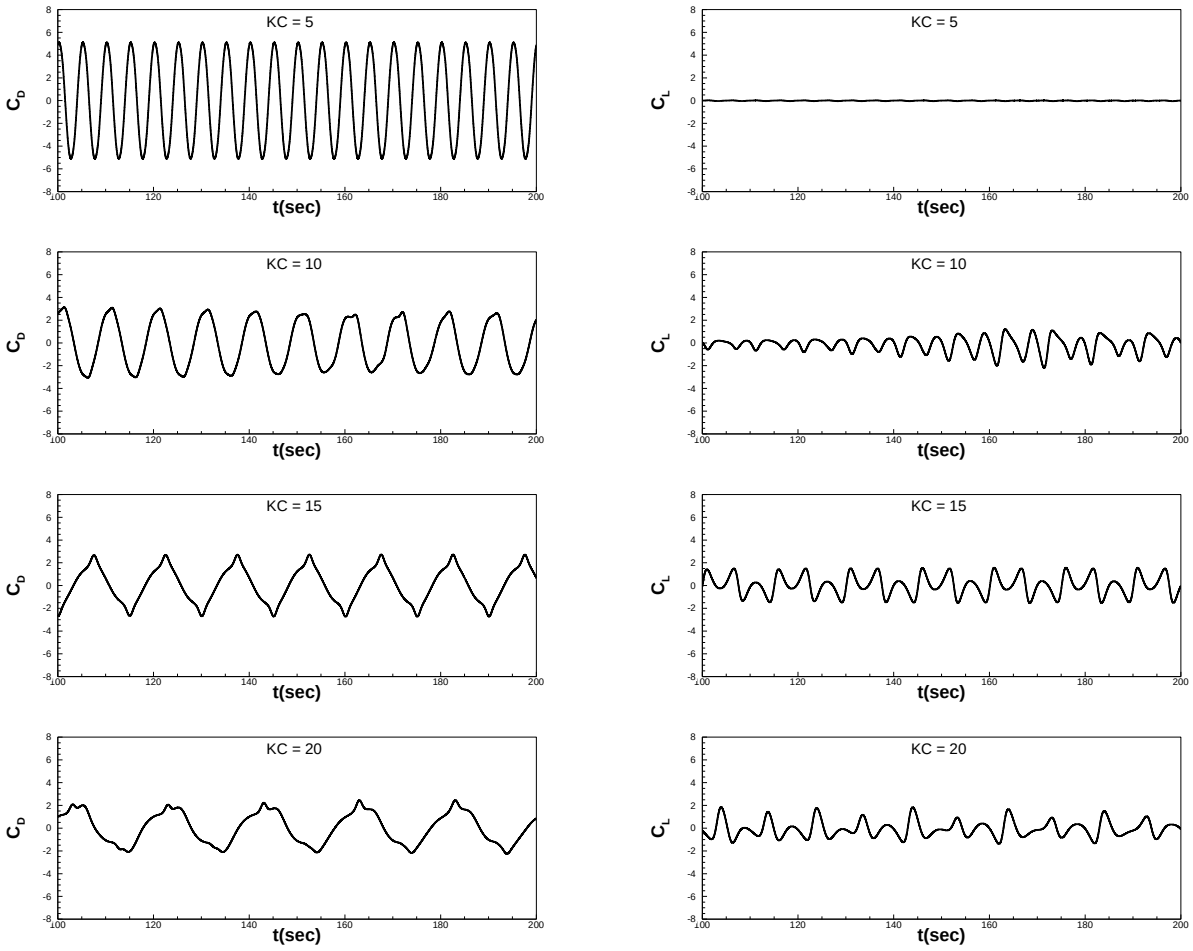

Figure 3. Time history of drag force coefficient (C_D) and lift force coefficient (C_L) for various KC values

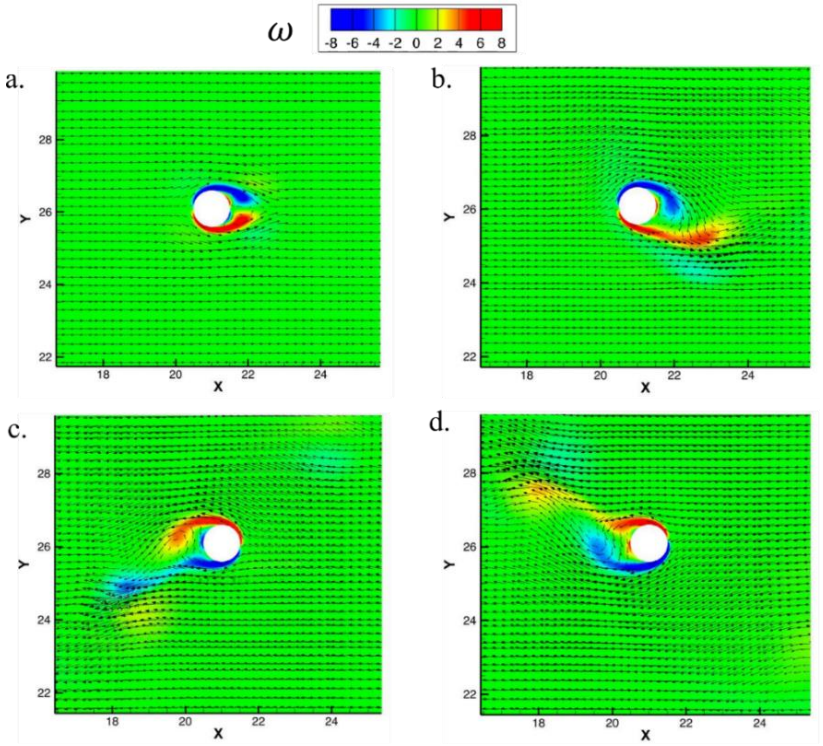

Figure 4. Instantaneous vorticity field (ω) for (a) KC=5; (b) KC=10; (c) KC=15 and (d) KC=20

3.2. Time History of Cylinder Displacements for Various KC Number

Figure 5 exhibits the dynamic response of a cylinder subjected to oscillatory flow at Keulegan–Carpenter (KC) = 5 for the range $5 \leq U_R \leq 35$. The objective is to analyze the displacement patterns in the in-line (x^*) and transverse (y^*) directions, as well as the interaction between the two, using a comparative approach between U_R values. The data analyzed are time series of vibration responses induced by oscillatory flow, which are shown in Figure 5.

For KC=5, the vibration displacement on both axes is relatively small compared to cases with larger KC values, and the response pattern changes in line with the increase in U_R. In general, there is an increase in transverse displacement (y^*) with a peak value at the beginning of the range, then decreasing for higher $U_R$values. The in-line vibration displacement response (x^*) is relatively more moderate throughout the range, without dramatic displacement spikes, so that the oscillation tends to dominate the transverse component at low KC. This observation can be seen from the shape and displacement in the time domain in each graph.

The displacement y^*reaches its maximum value in the initial U_R range ($U_R = 5$). Its magnitude is on the order of 5x10^{-2} (non-dimensional), reflecting a dominant cross-flow response even though KC is small. A relatively narrow and localized lock-in region is detected around U_R. In this zone, the y^*response is more periodic and the displacement increases over time until it reaches a maximum value that is maintained over time, indicating synchronization between the structural frequency and the frequency of the oscillatory flow excitation. The relationship between displacement and U_R at KC = 5 does not show a strong upper/lower bifurcation typical of steady flow VIV; the pattern is more similar to a relatively narrow single resonant peak. At high U_R ($U_R > 15$), a galloping phenomenon occurs where the y^*displacement decreases after lock-in and then increases relatively small but with a larger period and frequency response.

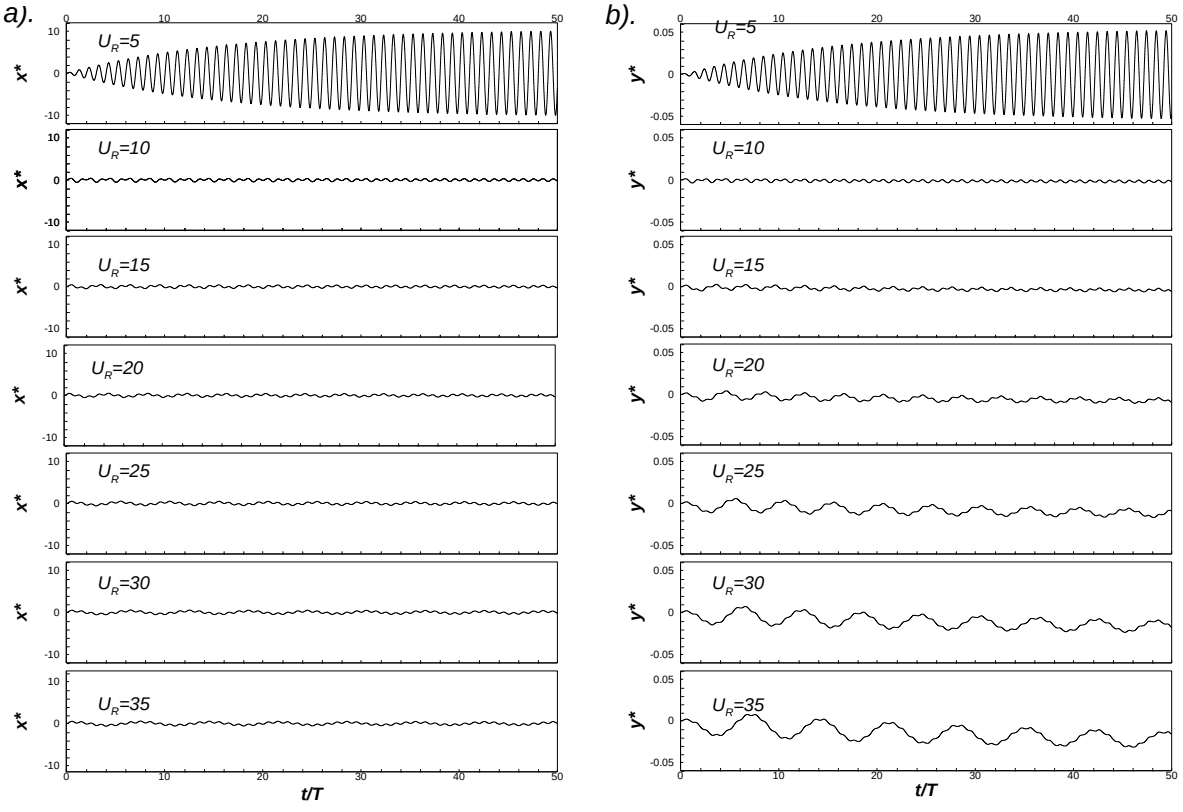

Figure 5. Time history of vibration displacement of a cylinder induced by oscillatory flow at KC number equal to 5 for various reduced velocity for (a) in-line and (b) transverse directions

The displacement response $x^*$is much greater than the response y^*in lock-in. In-line oscillations tend to dominate over transverse oscillations at KC = 5 due to the more dominant influence of flow compared to vortex shedding, which is not visible, and there is insignificant asymmetry at KC = 5. At high U_R, there is no slight increase in the response x^*as seen in the response y^*.

The phase relationship between $x^*$and y^* during the resonant region approaches a phase difference of approximately ±90°, consistent with a pattern indicating strong dynamic coupling between degrees of freedom in lock-in conditions. Outside of lock-in, the phase changes more freely and the coupling pattern weakens.

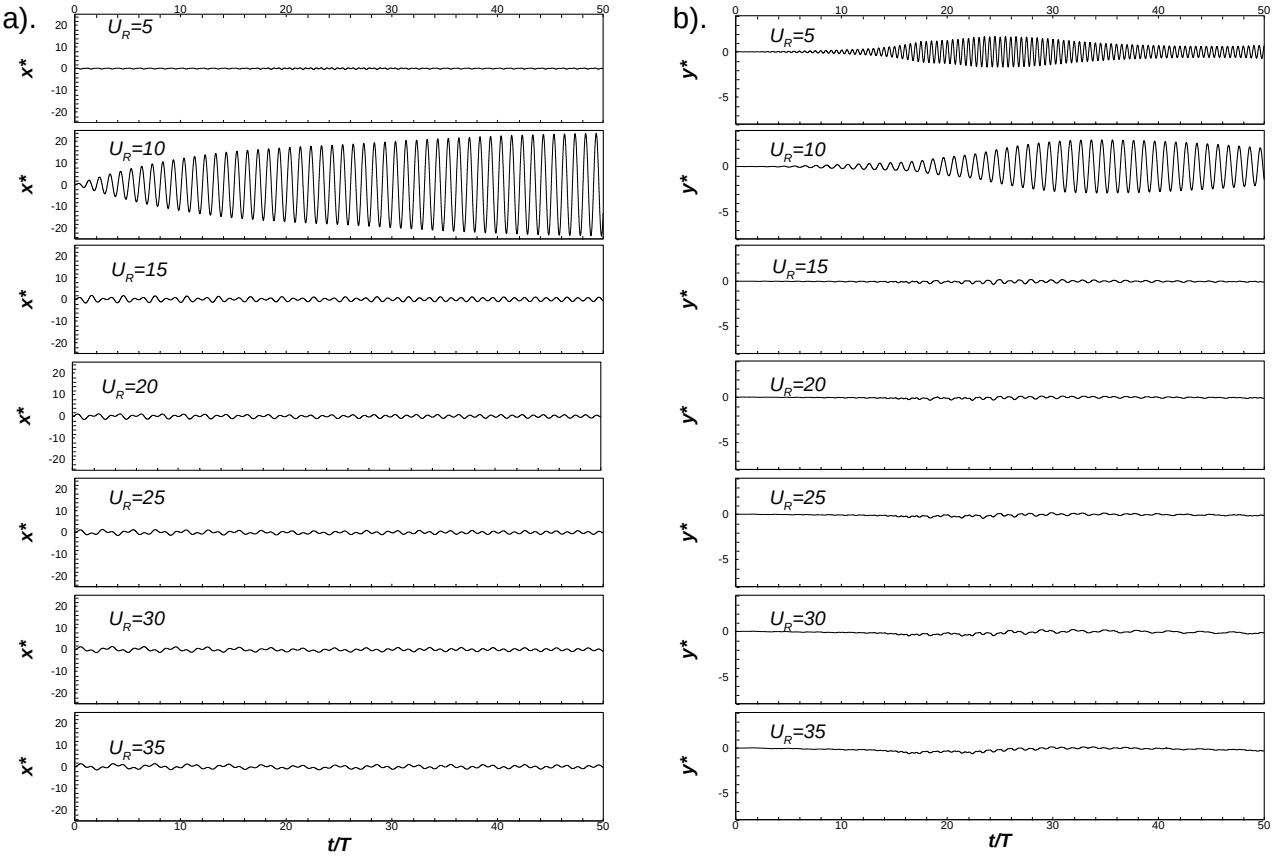

Figure 6. Time history of vibration displacement of a cylinder induced by oscillatory flow at KC number equal to 10 for various reduced velocity for (a) in-line and (b) transverse directions

The time history of dynamics response of the cylinder subjected to the oscillatory flow at KC=10 depicted in Figure 6. At KC = 10, the structural response shows significant displacement variation with increasing U_R. In general, the x^* response is more dominant than y^*. The x^*response has a small magnitude in the range $U_R = 5$, then spikes and reaches a peak value around $U_R = 10$, before decreasing again at higher U_R. In contrast, the y^*response shows more complex oscillations with displacement variations over time and there are indications of a beating phenomenon in the y^*response.

The maximum x^*response is achieved at $U_R = 10$, with relatively stable oscillations, indicating a strong lock-in phenomenon. In this range, the x^*response frequency is locked to the flow oscillation frequency, resulting in a regular response. The lock-in width at KC = 10 has the same pattern as KC = 5, indicating that KC further strengthens transverse oscillations. The displacement vs. U_R curve pattern shows indications of "upper branch" and "lower branch" branching, although not as classic as the VIV pattern in steady flow. The y^* response has a larger displacement compared to x^* at

$U_R = 5$, where the y^*motion dominates the system. However, when $U_R$is in the lock-in region ($U_R = 10$), the x^* displacement shows a pattern of correlation with the y^* motion, where both responses have maximum displacement values in the lock-in region. The phase relationship between x^* and y^* at $U_R = 10$ has a phase difference approaching 180°. These results confirm that at KC = 10, the x^* and y^*responses are stronger in the lock-in region, resonance amplification occurs, and vortex shedding phenomena are observed at KC=10, indicated by stronger transverse vibration responses compared to when KC=5.

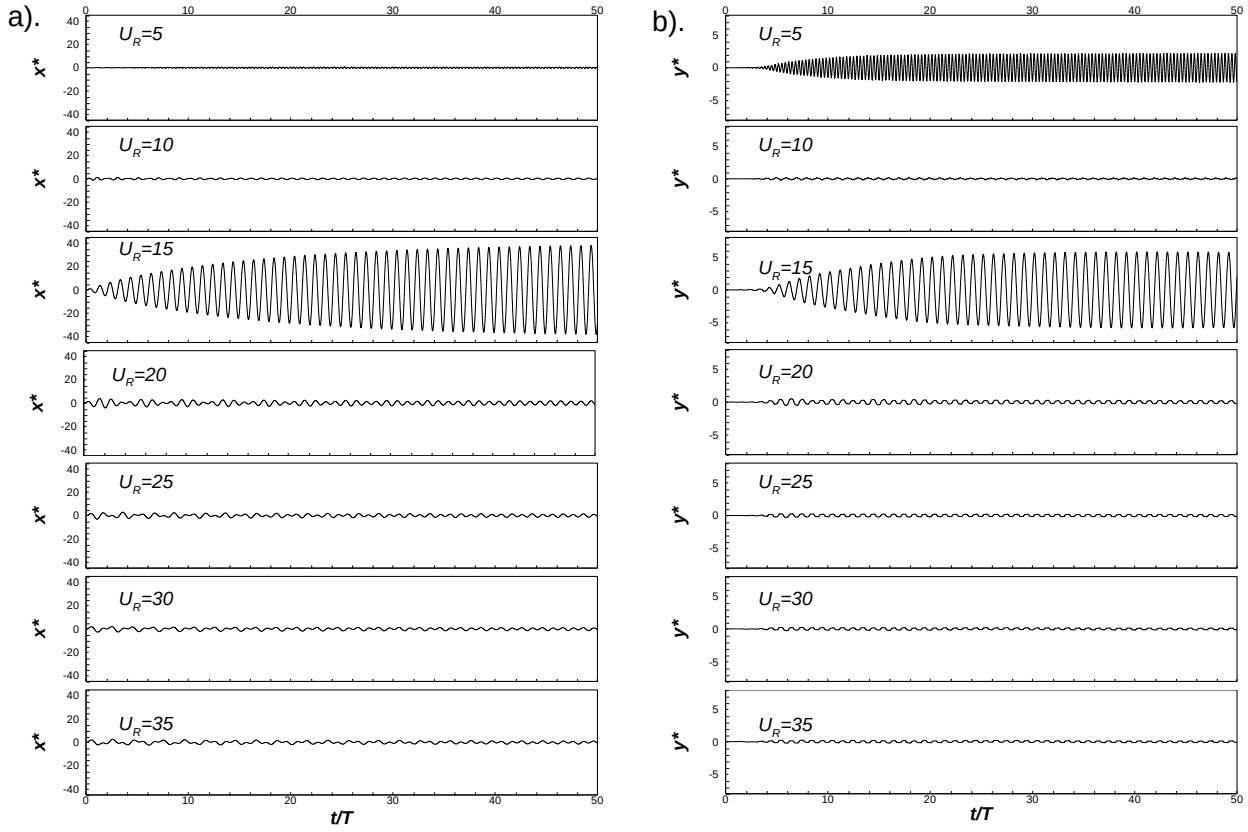

Figure 7. Time history of vibration displacement of a cylinder induced by oscillatory flow at KC number equal to 15 for various reduced velocity for (a) in-line and (b) transverse directions

Based on the analysis of Figure 7, time history displacement at KC = 15, it can be observed that the dynamic response of cylinders $x^*$and y^*shows significant dependence on variations in U_R. At low U_R values ($U_R = 5$), the vibration displacement in both directions is relatively small, with an x^*dynamic response that is almost undetectable, indicating that the oscillation flow at that U_R value is not sufficient to trigger a significant structural response. There is a slight anomaly in the y^*response where there is a decrease in the displacement of the y^*response from the $U_R$range of 5 to 10. As $U_R$increases, there is a noticeable growth in the displacement of x^*, with the peak displacement of in-line and transverse reaching around $U_R = 15$. This indicates the occurrence of the lock-in phenomenon, where the vortex shedding frequency synchronizes with the natural frequency of the structure, allowing for optimal energy transfer from the flow to the cylinder.

After the peak value occurs at $U_R = 15$, the vibration displacement gradually decreases as U_R increases. At $U_R = 20$, the decrease in $x^*$and y^* becomes clearly visible, while the x^* response remains significant compared to y^*even though

it tends to decrease. When U_R reaches 20, the dynamic responses of $x^*$and y^*return to very low levels, while the dynamic response of $x^*$is still observable, albeit with greatly reduced intensity. This pattern indicates that the system has exited the lock-in region, where the vortex shedding frequency is no longer synchronous with the natural frequency of the structure.

In general, for KC = 15, the dynamic response x^* is consistently greater than the dynamic response y^* across almost the entire U_R range, indicating the dominance of drag and inertia forces in moving the cylinder in the direction of flow. In addition, the shape of the vibration signal under lock-in conditions ($U_R = 15$) shows high stability and periodicity, indicating the occurrence of controlled resonance.

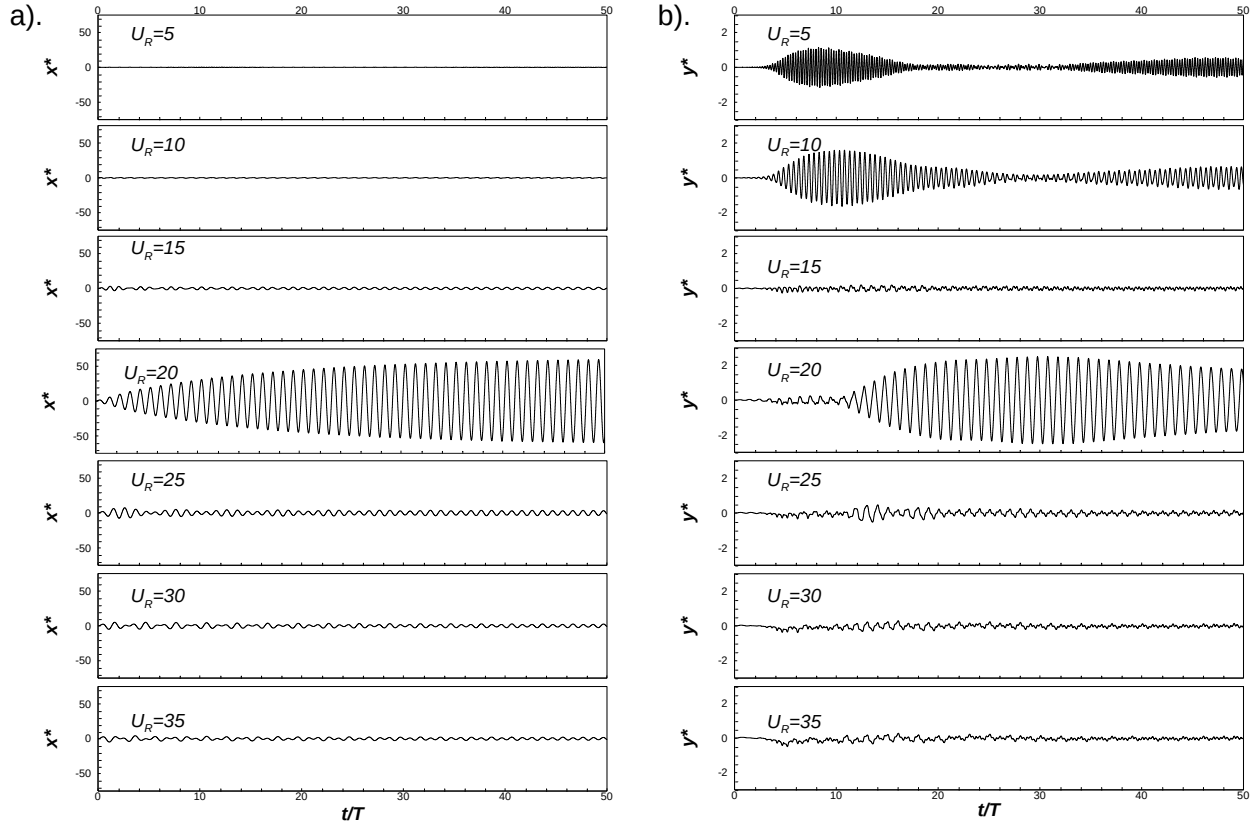

Figure 8. Time history of vibration displacement of a cylinder induced by oscillatory flow at KC number equal to 20 for various reduced velocity for (a) in-line and (b) transverse directions

Based on the analysis of Figure 8. Time History Vibration at KC = 20, it can be observed that the dynamic response of cylinders $x^*$and y^*shows a significant dependence on variations in U_R. At low $U_R$values ($U_R = 5$), the x^*vibration displacement is undetectable, indicating that the oscillation flow at that U_R value is not sufficient to trigger a meaningful structural response. There is an anomaly in the y^*response where a beating phenomenon occurs at U_R 5 and 10. As U_R increases, there is insignificant growth in the displacement of x^*, with the peak displacement in-line and transverse being achieved at $U_R = 20$. This indicates the occurrence of the lock-in phenomenon, where the vortex shedding frequency is synchronized with the natural frequency of the structure, so that the transfer of energy from the flow to the cylinder is optimal.

After the peak value occurred at $U_R = 20$, the vibration displacement experienced a significant reduction from $U_R = 20$ to $U_R = 25$. However, from $U_R = 25$ to $U_R = 35$, the vibration displacement did not experience a significant reduction. At $U_R = 20$, the decrease in $x^*$and y^* becomes clearly visible, while the x^*response remains significant

compared to y^*even though it tends to decrease. When U_R reaches 25, the dynamic responses of x^* and y^* return to very low levels, while the dynamic response of x^*can still be observed, albeit with greatly reduced intensity. This pattern indicates that the system has exited the lock-in region, where the vortex shedding frequency is no longer synchronous with the natural frequency of the structure.

In general, for KC = 20, the dynamic response $x^*$is consistently greater than the dynamic response y^* across almost the entire U_R range, indicating the dominance of drag and inertia forces in moving the cylinder in the direction of flow. In addition, the shape of the x^*graph under lock-in conditions ($U_R = 20$) shows high stability and periodicity, indicating controlled resonance. However, there is a difference in the pattern of the y^* response, where there is more than one peak displacement value of y^*, namely at $U_R = 10$ and $U_R = 20$, which indicates a significant vortex shedding effect at KC = 20.

VIV is produced, unlike in steady flow conditions, when the vortex shedding frequency matches the natural frequency of the structure (a phenomenon also known as lock-in) [1], [3], [20-21]. However, in oscillatory flow, the frequency due to oscillation of the incoming flow is the main determinant of the VIV regime. Resonant amplification and large vibration amplitudes follow when the imposed oscillatory frequency approaches the natural frequency of the structure. As the rate of the external vibration is already known and controlled, the beginnings of VIV in oscillatory flow are easier to predict than in the steady-flow context where the shedding of vortex arises by the flow field in a dynamic fashion. As a result, the VIV behavior in the case of oscillatory flow conditions is more predictable due to the direct relationship between the frequency of the excitation of the flowing system and the structural response.

In theory transverse vibrations are not expected to occur in oscillatory flow when KC numbers are low (KC < 10) [22-23], since the most common type of vortices generated by the flow field do not affect the flow structure at all in their net effect (see Figure 4). In this case, the hydrodynamic excitation across the flow is usually insignificant. However, with an elastically mounted cylinder, small asymmetries in the instantaneous velocity field may enhanced through fluid structure interaction. This way, transverse vibrations can still be measured at relatively low KC values.

3.3. Maximum Displacement of The Cylinder Subjected To Oscillatory Flow

Figure 9 represents the fundamental relationship between Reduced Velocity (U_R) and the structural response of a cylinder immersed in an oscillatory flow. Specifically, the graph depicts the maximum displacement value of the cylinder in the direction transverse to the flow (y^*_{max}), for four variations of the KC number (KC = 5, 10, 15, and 20). The objective is to identify vibration amplification characteristics, determine lock-in (frequency locking), and understand the influence of fluid-structure interaction in various flow regimes, all of which are critical information for the design and reliability analysis of offshore structures.

At KC = 5 (Figure 9 (a)), the response is dominated by a single displacement peak at $U_R = 5$, which then decreases sharply. However, when U_R increases further, the displacement no longer decreases but instead grows gradually until $U_R \approx 60$. This phenomenon indicates galloping, which is hydrodynamic instability that develops continuously as speed increases, unlike pure VIV patterns where the displacement is limited to the lock-in region.

At KC = 10 (Figure 9 (b)), the pattern becomes more complex with two main peaks. The first peak appears at $U_R = 5$, while the second, larger peak occurs at $U_R = 10$. After this secondary peak, the displacement decreases, then gradually increases again at high U_R. The presence of two peaks indicates a combination of synchronization (lock-in) as the primary peak and the vortex shedding effect that produces the secondary peak.

At KC = 15 (Figure 9 (c)), the displacement y^*max is much greater than the previous KC, with two significant peaks: a small peak at $U_R = 5$ and a sharp main peak at $U_R = 15$. After this peak, the transverse response weakens dramatically. This confirms that synchronization at $U_R = 15$ becomes dominant, and the vortex shedding effect widens the response range.

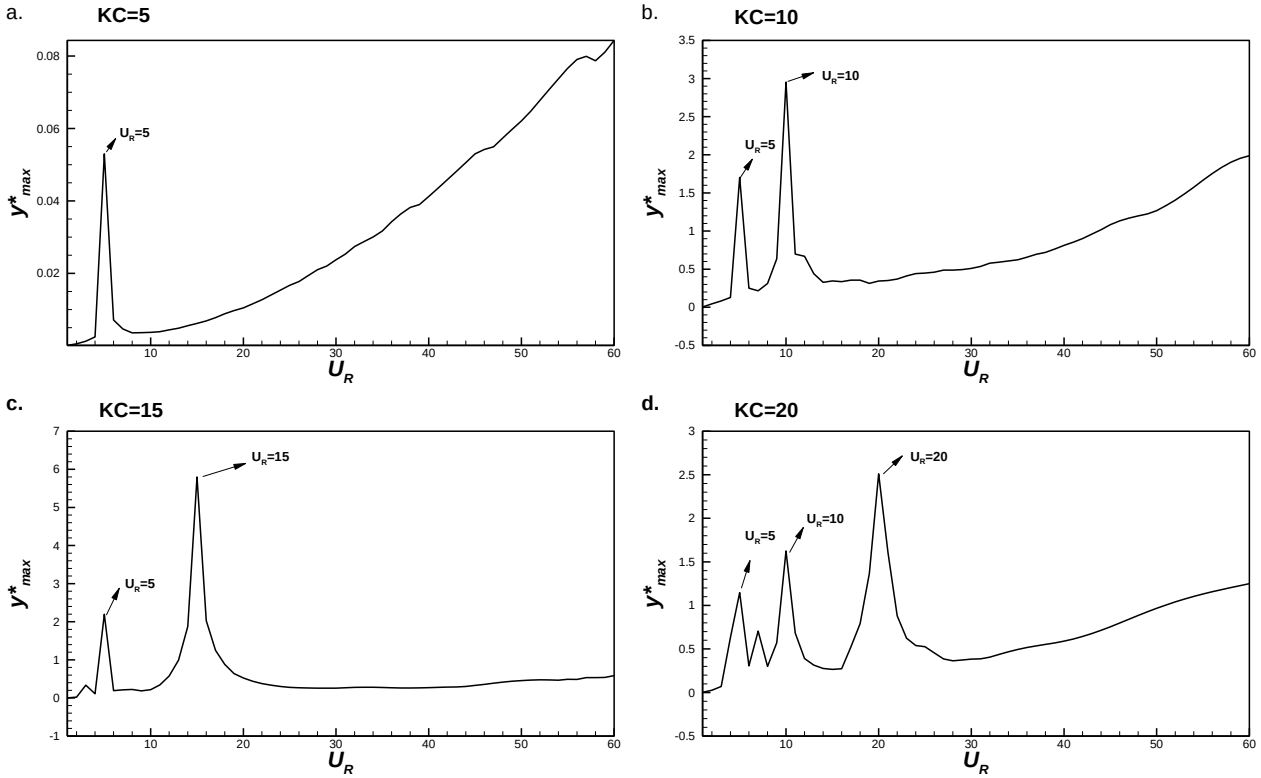

Figure 9. Maximum vibration displacement in transverse direction induced by oscillatory flow at (a. KC=5; b. KC=10; c. KC=15; and d. KC=20

At KC = 20 (Figure 8d), the pattern again shows several peaks, namely at $\boldsymbol{U_R = 5, 10, \text{and } 20}$. The displacement is not as high as KC = 15, but it is clear that increasing KC enriches the interaction mechanism, with more than one vibration mode being excited. As with KC = 10 and 15, the primary peaks are associated with synchronization (lock-in), while the secondary peaks originate from vortex shedding interactions that amplify oscillations at specific $\boldsymbol{U_R}$ values.

3.4. Conclusion

This study numerically investigated the two-degree-of-freedom (2-DoF) flow-induced vibration (FIV) response of a circular cylinder subjected to oscillatory flow, focusing on the interaction between reduced velocity (UR) and Keulegan–Carpenter (KC) numbers. The simulation results demonstrated that both parameters strongly influence vibration characteristics, including amplitude, frequency, and coupling between in-line and cross-flow motions.

For each KC value, a distinct lock-in region was identified, where the structural vibration frequency synchronized with the oscillatory flow excitation. The peak dynamic response occurred at $\boldsymbol{U_R}$ = 5, 10, 15, and 20 for KC = 5, 10, 15, and 20, respectively. As KC increased, the vibration pattern evolved from single-frequency to multi-mode behavior, accompanied by nonlinear coupling effects and phase shifts between the two motion directions. At higher $\boldsymbol{U_R}$ values, a galloping phenomenon was observed, indicating a transition from VIV to hydrodynamic instability.

The current results should be furthered in future research by researching on the impacts of different Reynolds number, mass ratios, the degree of structural damping, and non-harmonic or non-regular flows caused by waves would bring more insightful results on the actual ocean phenomenon. Furthermore, the fluid structure interaction model could be coupled with energy extraction mechanisms (i.e. power take-off (PTO) systems) to allow analysis onto the energy-harvesting performance of the fluid-structure interaction model in various KC and relative velocity ($\boldsymbol{U_R}$) regimes. It is also advisable that experimental validation in controlled oscillatory flow facilities be carried out to further confirm the numerical predictions as well as to adjust the modeling assumptions. The implication of the research is applicable in terms of both structural safety and renewable energy usage. The results, explain the combined effect of KC and $\boldsymbol{U_R}$ on vibration regimes, lock-in behavior, and galloping transition, help to enhance the prediction of fatigue loads on offshore risers, mooring lines and submerged cylindrical components. Moreover, knowledge of these flow induced vibration properties (KC-$\boldsymbol{U_R}$ coupling parameters) can be used in designing and optimization of oscillatory-flow-based energy-harvesting systems, which can facilitate better harvesting of marine renewable energy in a more efficient and predictable manner.

Acknowledgement

The authors gratefully acknowledge the financial support provided by Politeknik Negeri Semarang, through the Penelitian Terapan Kompetitif from P3M. This support was essential for the successful completion of this research.

References

[1] X. Sun, Y. X. Zhang, M. M. Tao, D. X. Han, and J. Xiao, "Vortex-induced rotational vibration of an eccentric circular cylinder at low Reynolds number of 100," *Nonlinear Dyn*, vol. 111, no. 16, pp. 14805–14828, Aug. 2023, doi: 10.1007/s11071-023-08648-8.

[2] H. jie Wen, Y. meng Zhao, G. cheng Zhu, L. sheng Zhu, and B. Ren, "SPH Modelling of the Vortex-Induced Vibration of A Near-Wall Cylinder," *China Ocean Engineering*, vol. 37, no. 3, pp. 355–368, Jun. 2023, doi: 10.1007/s13344-023-0030-6.

[3] L. Jia, S. Sang, X. Shi, and F. Shen, "Investigation on Numerical Simulation of VIV of Deep-Sea Flexible Risers," *Applied Sciences (Switzerland)*, vol. 13, no. 14, Jul. 2023, doi: 10.3390/app13148096.

[4] R. Li *et al.*, "Numerical Investigation of Vortex-Induced Vibrations of a Rotating Cylinder near a Plane Wall," *J Mar Sci Eng*, vol. 11, no. 6, Jun. 2023, doi: 10.3390/jmse11061202.

[5] Y. Jang, H. Kim, C. M. Lee, S. B. Suh, and I. Lee, "Effect of the geometric configuration of the pendulum system of tandem cylinders (PSTC) on the hydrokinetic energy conversion efficiency of wake-induced vibration," *Journal of Mechanical Science and Technology*, vol. 37, no. 2, pp. 779–791, Feb. 2023, doi: 10.1007/s12206-023-0121-6.

[6] Z. B. Hu *et al.*, "Experimental Study on Vortex-Induced Vibration of Rough Risers Coupling with Interference Effect in Tandem Arrangement," *China Ocean Engineering*, vol. 38, no. 3, pp. 394–407, Jun. 2024, doi: 10.1007/s13344-024-0032-z.

[7] Z. B. Hu *et al.*, "Experimental Study on Vortex-Induced Vibration of Rough Risers with Coupling Interference Effect Under Side-by-Side Arrangement," *China Ocean Engineering*, vol. 38, no. 1, pp. 18–28, Feb. 2024, doi: 10.1007/s13344-024-0002-5.

[8] P. Han, E. De Langre, M. C. Thompson, K. Hourigan, and J. Zhao, "Vortex-induced vibration forever even with high structural damping," *J Fluid Mech*, vol. 962, May 2023, doi: 10.1017/jfm.2023.268.

[9] G. Qin, H. Zhang, and D. Li, "Vortex-Induced Vibration and Frequency Lock-In of an Elastically Suspended Hydrofoil with Blunt Trailing Edge," *J Shanghai Jiaotong Univ Sci*, 2024, doi: 10.1007/s12204-023-2693-9.

[10] A. Joy, V. Joshi, K. Narendran, and R. Ghoshal, "Piezoelectric energy extraction from a cylinder undergoing vortex-induced vibration using internal resonance," *Sci Rep*, vol. 13, no. 1, Dec. 2023, doi: 10.1038/s41598-023-33760-5.

[11] H. Huang, Z. Zhou, P. Zhu, W. Qin, and W. Du, "Enhancing energy harvesting through hybrid bluff body at a predefined angle of attack coupling vortex-induced vibration and galloping," *Ocean Engineering*, vol. 312, Nov. 2024, doi: 10.1016/j.oceaneng.2024.119029.

[12] H. Li, S. Li, Q. Ding, H. Xiong, and X. Kong, "An electromagnetic vibro-impact nonlinear energy sink for simultaneous vibration suppression and energy harvesting in vortex-induced vibrations," *Nonlinear Dyn*, vol. 112, no. 8, pp. 5919–5936, Apr. 2024, doi: 10.1007/s11071-024-09380-7.

[13] S. Fan, Z. Li, J. Song, X. Du, and J. Wang, "Effects of Angle of Attack on Flow-Induced Vibration of a D-Section Prism," *J Mar Sci Eng*, vol. 12, no. 7, Jul. 2024, doi: 10.3390/jmse12071235.

[14] L. Liu, Y. Yu, and Y. Chen, "Wind-Vortex-Induced Vibrations of a Deepwater Jacket Pipe and Vibration Suppression Using a Nonlinear Energy Sink," *Journal of Ocean University of China*, vol. 23, no. 3, pp. 633–642, Jun. 2024, doi: 10.1007/s11802-024-5666-1.

[15] E. Basta, S. K. Gupta, and O. Barry, "Frequency lock-in control and mitigation of nonlinear vortex-induced vibrations of an airfoil structure using a conserved-mass linear vibration absorber," *Nonlinear Dyn*, vol. 112, no. 11, pp. 8789–8809, Jun. 2024, doi: 10.1007/s11071-024-09543-6.

[16] H. He, J. Wang, and F. Wang, "Investigation of the Effects of Vortex Isolation Plates with Different Opening Ratios and Sizes on Vortex-Induced Vibration," *Applied Sciences (Switzerland)*, vol. 14, no. 9, May 2024, doi: 10.3390/app14093863.

[17] M. Islam, U. Ali, and S. Mone, "Harnessing flow-induced vibrations for energy harvesting: Experimental and numerical insights using piezoelectric transducer," *PLoS One*, vol. 19, no. 6 June, Jun. 2024, doi: 10.1371/journal.pone.0304489.

[18] J. Li and N. Z. Chen, "Vortex-Induced Vibration (VIV) of flexible riser conveying severe slugging and straight flow in steady and oscillatory flows," *J Sound Vib*, vol. 595, no. September 2024, p. 118728, 2025, doi: 10.1016/j.jsv.2024.118728.

[19] Y. Huang, S. Cao, D. Cao, and Q. Yang, "In-line force modeling for a circular cylinder in oscillatory flow with non-zero mean velocity," *Journal of Wind Engineering and Industrial Aerodynamics*, vol. 262, no. April, p. 106109, 2025, doi: 10.1016/j.jweia.2025.106109.

[20] A. An-Nizhami, N. Apriandi, A. Sai'in, P. Yanuar, W. I. Nugroho, and E. R. Riadini, "Fluid-Structure Interaction Medelling for Vibration Energy Extraction from A Circular Cylinder In Cross-Flow," *Journal of Engineering Science and Technology*, vol. 19, no, 2, pp. 83-97, 2024, doi: https://jestec.taylors.edu.my/Special%20Issue%20ICIST%202023/ICIST_08.pdf.

[21] A. An-Nizhami *et al.*, "Mass Ratio Influence on Vortex-Induced Vibration of a Flexible Cylinder using Large Eddy Simulation at Re=1000," *Journal of Mechanical Engineering and Applied Technology*, vol. 2, no. 1, pp. 43–50, 2023.

[22] L. Shen, E. S. Chan, and P. Lin, "Calculation of hydrodynamic forces acting on a submerged moving object using immersed boundary method," *Comput Fluids*, vol. 38, no. 3, pp. 691–702, 2009, doi: 10.1016/j.compfluid.2008.07.002.

[23] H. Dütsch, F. Durst, S. Becker, and H. Lienhart, "Oscillating Circular Cylinder At Low Keulegan–Carpenter numbers," *J Fluid Mech*, vol. 360, pp. 249–271, 1998.